

www.acsami.org Research Article

Observation of Sub-10 nm Transition Metal Dichalcogenide Nanocrystals in Rapidly Heated van der Waals Heterostructures

Pawan Kumar, Jiazheng Chen, Andrew C. Meng, Wei-Chang D. Yang, Surendra B. Anantharaman, James P. Horwath, Juan C. Idrobo, Himani Mishra, Yuanyue Liu, Albert V. Davydov, Eric A. Stach,* and Deep Jariwala*



Cite This: ACS Appl. Mater. Interfaces 2023, 15, 59693-59703



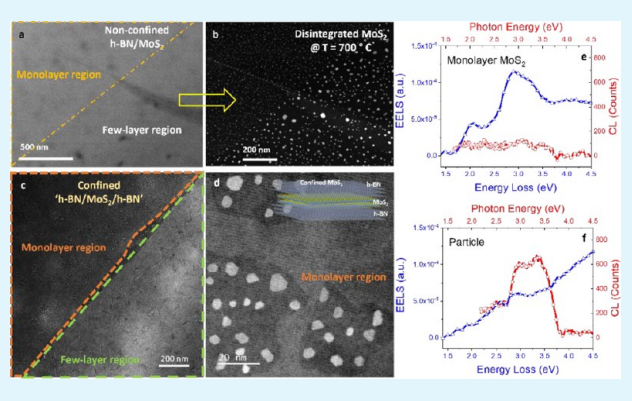
ACCESS

Metrics & More

Article Recommendations

Supporting Information

ABSTRACT: Two-dimensional materials, such as transition metal dichalcogenides (TMDCs), have the potential to revolutionize the field of electronics and photonics due to their unique physical and structural properties. This research presents a novel method for synthesizing crystalline TMDCs crystals with <10 nm size using ultrafast migration of vacancies at elevated temperatures. Through *in situ* and *ex situ* processing and using atomic-level characterization techniques, we analyzed the shape, size, crystallinity, composition, and strain distribution of these nanocrystals. These nanocrystals exhibit electronic structure signatures that differ from the 2D bulk: i.e., uniform mono- and multilayers. Further, our *in situ*, vacuum-based synthesis technique allows observation and comparison of defect and phase evolution in these crystals formed under van der Waals



heterostructure confinement versus unconfined conditions. Overall, this research demonstrates a solid-state route to synthesizing uniform nanocrystals of TMDCs and lays the foundation for materials science in confined 2D spaces under extreme conditions.

KEYWORDS: 2D Materials, in situ, Electron Microscopy, 4D-STEM, EELS, Cathodoluminescence, Scanning Probe microscopy

INTRODUCTION

Research into the one-dimensional (1D) and zero-dimensional (0D) confinements of two-dimensional (2D) materials has been ongoing for some time. 1,2 Various successful approaches have been employed, such as electrostatic confinement, defect creation, modulation of band gaps through composition in lateral heterostructures, and strain-induced band gap modulation.³⁻⁶ However, crafting uniform, sub-10 nm crystalline structures of transition metal dichalcogenides (TMDCs) using a top-down process continues to pose a significant challenge. To date, TMDC-based nanoparticles have been synthesized through either top-down or bottom-up approaches. Bottom-up approaches have utilized precursor concentration control as well as biomineralization approaches to form quantum dots (QDs), while the top-down approaches exploit electrostatic confinement via nanofabrication of metal gates on 2D layers or decomposition from bulk TMDC crystals under sonication in the presence of surfactants. 8-10 Among the existing bottom-up techniques, maintaining control over the particles' crystallinity, size, and defects can be difficult. Similarly, the top-down techniques that are currently available still face the ongoing challenge of ensuring scalability and managing the control of the phase and defects.

In this study, we present a unique approach to fabricating 2–15 nm lateral size particles through nonequilibrium

thermolysis of 2D materials, resulting in the formation of nanocrystals that maintain the crystallinity of the starting single crystalline flake. In situ and ex situ processing along with atomic-level characterization techniques such as aberrationcorrected scanning transmission electron micro-spectroscopy and scanning probe micro-spectroscopy were used to analyze the shape, size, crystallinity, composition, and strain distribution of these nanocrystals. The electronic structure signatures of these nanocrystals, which differ from those of bulk materials, were also studied using near-field photoluminescence (PL), cathodoluminescence (CL), and electron energy loss spectroscopy (EELS). Our vacuum-based synthesis technique allows for the observation and comparison of defect and phase evolution under nanoscopic confinement vs open conditions. Overall, this study presents a solid-state route to synthesizing uniform nanocrystals of TMDCs and lays the foundation for

Received: September 11, 2023 Revised: November 15, 2023 Accepted: November 20, 2023

Published: December 13, 2023





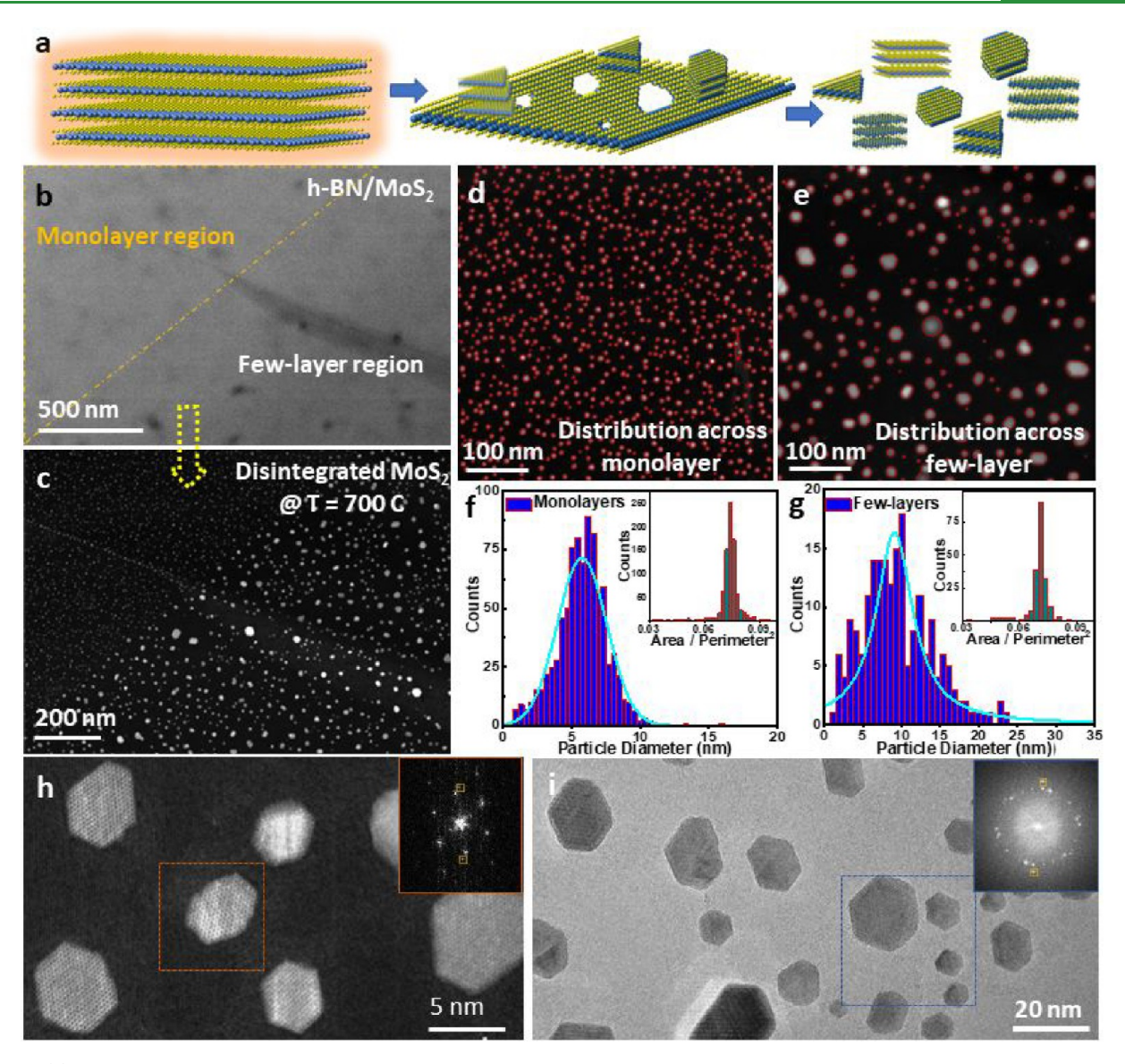


Figure 1. (a) An atomic model illustrating the thermolysis process for the formation of crystalline sub-10 nm particles of MoS_2 of varying shapes. (b) Dark-field STEM image of a continuous monolayer and few-layer MoS_2 supported with h-BN prior to rapid heating (in situ) and thermolysis and corresponding (c) thermolysis-induced disintegration into crystalline nanoparticles from the parent continuous layer. (d, e) Magnified views of the disintegrated nanoparticles from the monolayer and few-layer regions which were used for the size and shape analysis. The particle size statistics were analyzed using convolutional neural network (CNN) based machine learning as presented in (f) and (g) for monolayer and few-layer regions, respectively. (h) Atomic resolution HAADF-STEM image of the disintegrated nanoparticles made from a monolayer region post in situ thermolysis. (i) Phase-contrast TEM image of the nanoparticles disintegrated from the few-layer region and corresponding FFT patterns (insets) extracted from the marked rectangular box regions in (h) and (i), respectively.

materials science in confined 2D spaces under extreme conditions.

There are many potential applications for nanocrystals and other confined structures synthesized from 2D materials. Interface bridging structures of different dimensionalities provide a unique opportunity for a wide variety of device applications. Some examples include logic devices, where confined materials provide opportunities to address challenges from scaling limits, and photodetectors, shall the optoelectronic properties of which can be modulated through interfacial chemistry. Nonequilibrium thermolysis of 2D materials provides a synthesis pathway for 2D/0D integration for more systematic studies of these devices. The method is also amenable to materials processing up to the micro/mesoscale,

allowing devices with larger areas compared to those made using localized defect creation.

■ RESULTS AND DISCUSSION

We demonstrate a novel method for fabricating TMDC nanocrystals via a thermolysis process, ¹⁵⁻¹⁷ in which an ultrafast increase in temperature (less than a few seconds) leads to the rapid formation of sub-10 nm particles. We have studied this transformation both *in situ*, using a microheater fabricated on a micro-electromechanical system (MEMS) transmission electron microscopy (TEM) chip, and *ex situ* in a tube furnace (see Materials and Methods for additional details).

Figure 1a shows an atomic model of the transformation of a continuous monolayer or few-layer TMDC into tiny islands

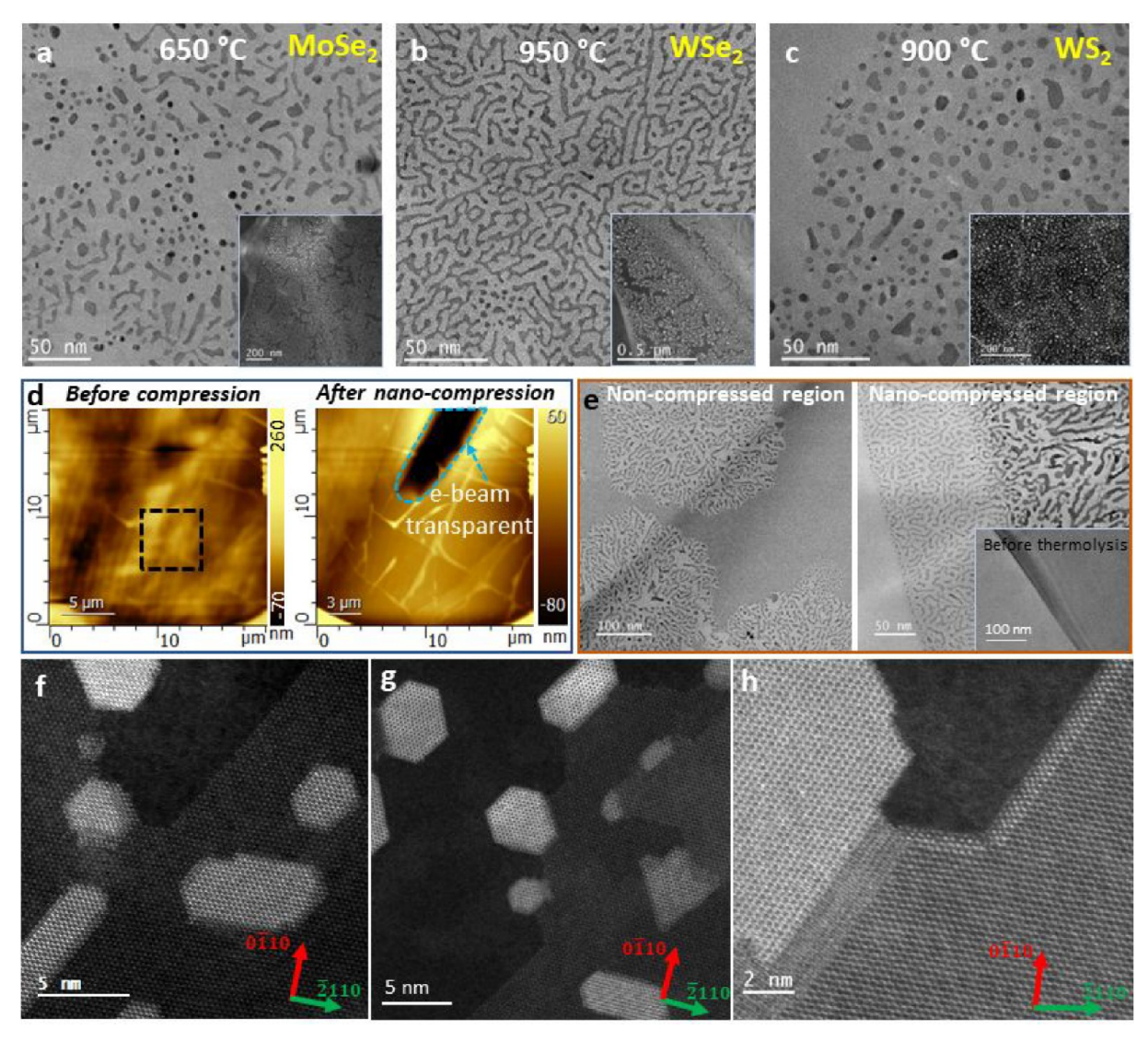


Figure 2. Bright-field TEM images of the (a) $MoSe_2$, (b) WSe_2 , and (c) WS_2 particles after thermolysis (in situ heating) at the respective temperatures. The insets show a lower magnification view of the transformed particles. (d) AFM height images of the transferred continuous WSe_2 layer before and after compression at the preheating stage. Nanocompression was performed using an AFM tip in contact mode (applying 1 μ N force) before height scanning. (e) Corresponding bright-field TEM images of the regions in (d) after rapid heating (in situ) showing how nanocompression forms better interfaces. (f, g) Atomically resolved HAADF-STEM images of the disintegrated particles showing layer-by-layer disintegration during thermolysis. (h) Atomic resolution HAADF-STEM image showing edge reconstruction, which was observed at some locations.

through rapid thermolysis. For in situ rapid thermolysis, the TMDC layer was transferred onto a microheater fabricated on a MEMS TEM chip (see Figure S1). To ensure uniform heat distribution to the TMDC layer, a highly thermally conducting h-BN support layer was utilized (Figure S2). Microholes were made in the SiNx membrane of the TEM chip using a focused ion beam (FIB), allowing for atomic resolution imaging of the 2D layers (see Figure S1e,f). Figure 1b shows a high-angle annular dark field (HAADF) scanning transmission electron microscopy (STEM) image of MoS₂ at room temperature, consisting of monolayer and few-layer structures, as highlighted in the image. After thermal processing, the formation of randomly distributed tiny islands can be seen in Figure 1c. The thickness dependence of this transformation is shown in the HAADF-STEM image, and two different particle size distributions are observed (see Figures S3 and S4 for details). Image segmentation and nanoparticle measurement details are

described in Materials and Methods. Figure 1d,e shows STEM micrographs corresponding to the thermolysis of monolayer and few-layer MoS₂, respectively. The corresponding size distribution histograms are shown in Figure 1f,g, with the fitting curve indicating that monolayer MoS₂ transformed into multilayered particles with a lateral size of approximately 4-6 nm, while few-layer MoS₂ transformed into particles with a size of approximately 10 nm. The particle size distributions fit approximately a Gaussian distribution with a mean of ~5 nm for the monolayer starting material, while a Lorentzian distribution curve provides a better description of the fewlayer starting material, with a median of \sim 10 nm. The ability to control the particle size through the control of the initial layer thickness allows for the design of various engineered nanostructures. The shape distribution analysis is also shown in the insets of Figure 1f,g (histogram view for area/ perimeter²) and in Figure S5, where a tendency to form two

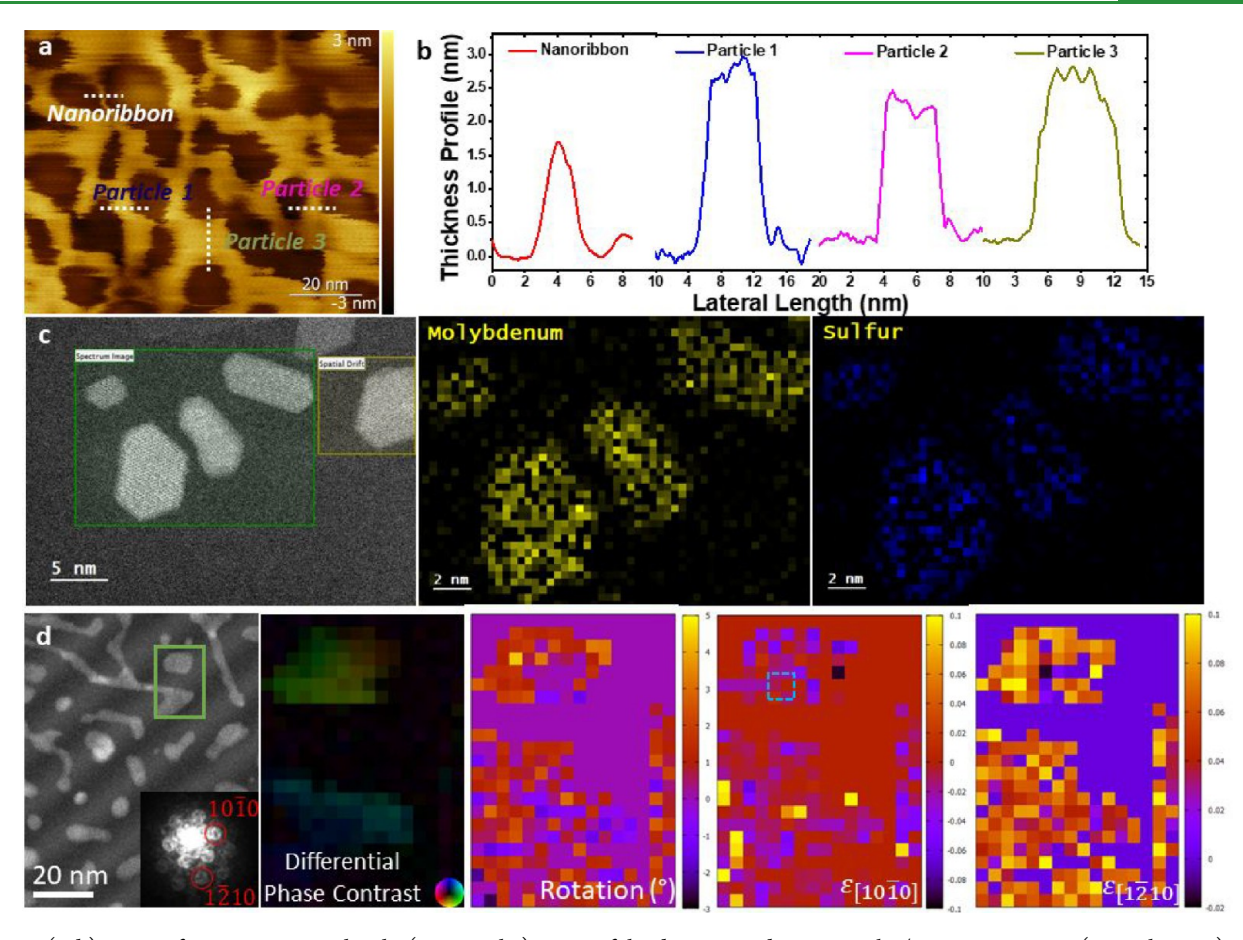


Figure 3. (a, b) Atomic force microscopic height (topography) image of the disintegrated nanoparticles/nanoconstrictions (in situ heating) and the corresponding line profile analysis. The data show clear formation of 4–10 nm wide multilayered (and up to 3 nm thick) particles and constrictions. (c) EDS elemental mapping (MoS₂) confirming the formation of stoichiometric nanoparticles. (d) 4D-STEM analysis of the disintegrated MoS₂ nanoparticles showing (left to right) a dark field STEM image, a differential phase contrast (DPC) image, and rotation and strain maps in two component directions, $[10\overline{1}0]$ and $[1\overline{2}10]$.

different shapes (with hexagon being the dominant shape) can be seen. Further, an atomically resolved HAADF-STEM image is shown in Figure 1h, which shows the nanoparticles after monolayer disintegration. We also analyze these nanocrystals in the phase contrast TEM image, as shown in Figure 1i. The FFT patterns extracted from the respective STEM and HR-TEM images (a rectangular box in a different color) are also shown as insets, highlighting the preserved hexagonal crystal symmetry after thermal disintegration. The FFT patterns presented as insets show that crystal orientations of different nanoparticles are not aligned with respect to each other. The other brighter spots (aside from the six streaks) marked rectangular in the FFT pattern correspond to the crystalline h-BN layer.

The formation of highly confined multilayered particles was also observed for other TMDCs such as MoSe₂, WSe₂, and WS₂. The as-formed crystalline particles from various TMDCs are shown in bright-field STEM images in Figure 2a–c, respectively, at different thermolysis temperatures. The inset lower magnification images provide a larger area view of the *in situ* transformed crystalline particle formation (see Figures S6 and S7 for more details). Selenium-based TMDCs mostly form connected chains of islands after thermolysis, while sulfurbased TMDCs form isolated particles. The decomposition of chalcogenides in a selenium-rich environment at raised temperatures is known to precipitate an amorphous-like

(fine-grain) layer consisting of selenium and carbon surrounding the larger crystallite (TMDC islands). The amorphous-like substance may tether the selenium-based TMDCs that experience thermolysis to form chains of islands.

While performing the in situ thermolysis process, a significant challenge is ensuring the successful and clean transfer of an atomically thin 2D layer over the SiN_x membrane due to polymer contamination. The dry transfer technique, which is the most feasible and widely used method for transferring multiple layers one after another, almost always leaves a thin polydimethylsiloxane (PDMS) residual layer (see Materials and Methods for details) even when performed in a glovebox after fresh exfoliation. This thin polymer layer forms agglomerated islands after annealing treatment (annealing at 300 °C under a forming gas environment for 8–12 h) following each layer transfer process. We observe that the PDMS residue at the interface of the h-BN and TMDC layers remaining from the stamp transfer process acts as a barrier layer, resulting in nonuniform heat spread during rapid thermolysis (see Figure S8). This nonuniformity can be eliminated by using the nanocompression technique²¹ before the thermolysis process. The atomic force microscopy (AFM) height image of the transferred h-BN/WSe₂ layer on the TEM grid before and after (Figure 2d) the nanocompression process clearly shows the flatness of the heterostructures (here, h-BN/ WSe₂). The trapped PDMS layer was removed from the

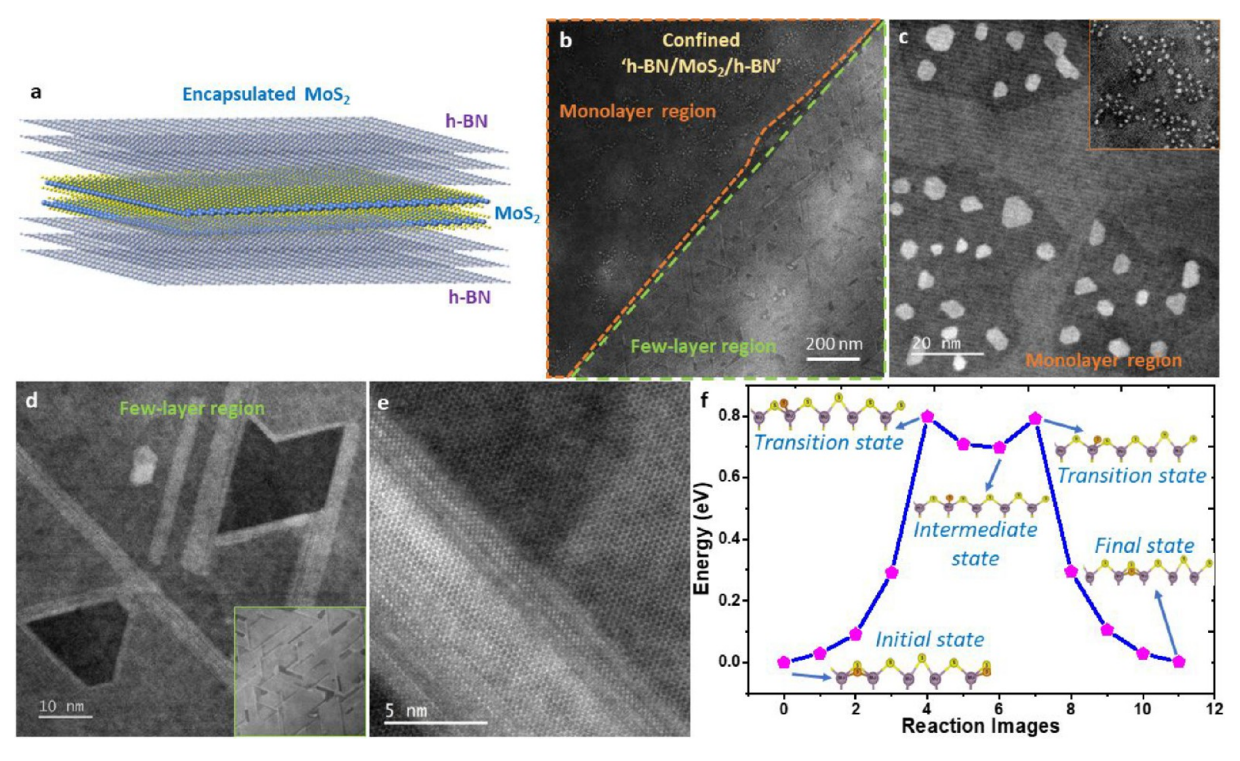


Figure 4. (a) Schematic showing the encapsulated 2D MX₂ TMDC layer between the top and bottom few-layer h-BN. (b) Dark-field STEM image of the disintegrated particles (in situ heating) under 2D encapsulation highlighting two different thicknesses as outlined by the orange and green dashed boundaries. (c) The corresponding high-resolution STEM image for the monolayer region showing pockets of disintegration with triangular and truncated hexagonal particles. (d) STEM image for the few-layer region, showing unique edge reconstruction and faceted-trench formation (see inset) unlike the monolayer case which disintegrated into geometric \sim 5 nm size particles under encapsulation. (e) Atomically resolved HAADF-STEM image of one of the as-formed restructured trenches showing the armchair-type edge atomic structure and the surrounding continuous region that has not disintegrated. (f) First-principles calculation of sulfur diffusion at the MoS₂ edge and the corresponding energy explaining the tendency of the differing shapes based upon stable edge formations under encapsulation.

interface using a sharp AFM tip to improve adhesion. ^{21,22} The microscopically flat and better-interfaced heterostructure (h-BN/WSe₂) layer leads to the uniform and complete transformation of the WSe₂ layer into sub-10 nm size islands compared to the noncompressed regions, as seen in Figure 2e. These compressed, flat regions are clearer to image in the electron-transparent region (visible bean-shaped regions in Figure 2d) available in the TEM grid, where all the in situ imaging was performed. In principle, the noncompressed regions can also be transformed into nanoparticles if the thermolysis time is increased to more than 10 s. However, the stoichiometry of the TMDC layer is lost, and metal nanocrystals begin to nucleate due to excessive loss of the chalcogen instead of leading to stoichiometric TMDC nanoparticle formation (see metal crystal formation in Figure S9d-f).

Nonequilibrium thermolysis relies on the rapid migration of vacancies, primarily S-vacancies in the case of MoS₂ or WS₂, to synthesize TMDC nanoparticles.¹⁷ While it can be challenging to observe the complete formation process in detail, we were able to confirm the different stages of the formation using atomic resolution HAADF-STEM images as shown in Figure 2f,g (also shown in Figures S10–S12). These images show layer-by-layer diffusion and the formation of nanoparticles in the few-layer TMDCs. We also observed edge reconstruction and phase transformation at some sites during the thermolysis process (Figure 2h). The edge reconstruction is mostly visible in cases where the temperature increase occurred at a slower rate than intended in the experiment. The corresponding FFT

(see Figures S10 and S11) confirms the similar orientation of the nanoparticles and layers underneath. Further, we characterized the nanoparticles using a range of tools, including AFM, STEM-EDS (energy dispersive X-ray spectroscopy), and 4D-STEM mapping. Figure 3a shows an AFM height image, with the corresponding line profiles being shown in Figure 3b. The particles or constrictions (nanoribbons) have thicknesses ranging from a bilayer (~1.7 nm) to a few layers (~3 nm) and lateral dimensions ranging from 3 to 10 nm. STEM-based EDS mapping, shown in Figure 3c, was used to analyze the elemental composition of the particles. The STEM image of the survey area and the marked green rectangle region show a uniform distribution of Mo and S elements (see Figure S13 for additional EDS images taken from a batch of samples). It is worth noting that EDS mapping at 200 kV may result in the loss of sulfur atoms due to knock-on damage during spectral imaging.²³ Relative crystallographic orientation changes can occur between nanoparticles formed from the MoS2 singlecrystal flakes (see Figure S14). 4D-STEM is used to perform differential phase contrast imaging (Figure 3d, #2) and to characterize strain (Figure 3d, #3-5) in the MoS₂ nanoparticles. Differential phase contrast (DPC) mapping is measured using the center of mass method, which is influenced by electromagnetic fields in the sample as well as sample crystallographic orientation.^{24,25} Figure 3d (#2) indicates slight DPC in the MoS₂ particles: this can arise due to an electromagnetic field in the material, strain differences, crystallographic orientation differences, or a combination of all three. The strain maps show that the lattice parameter of

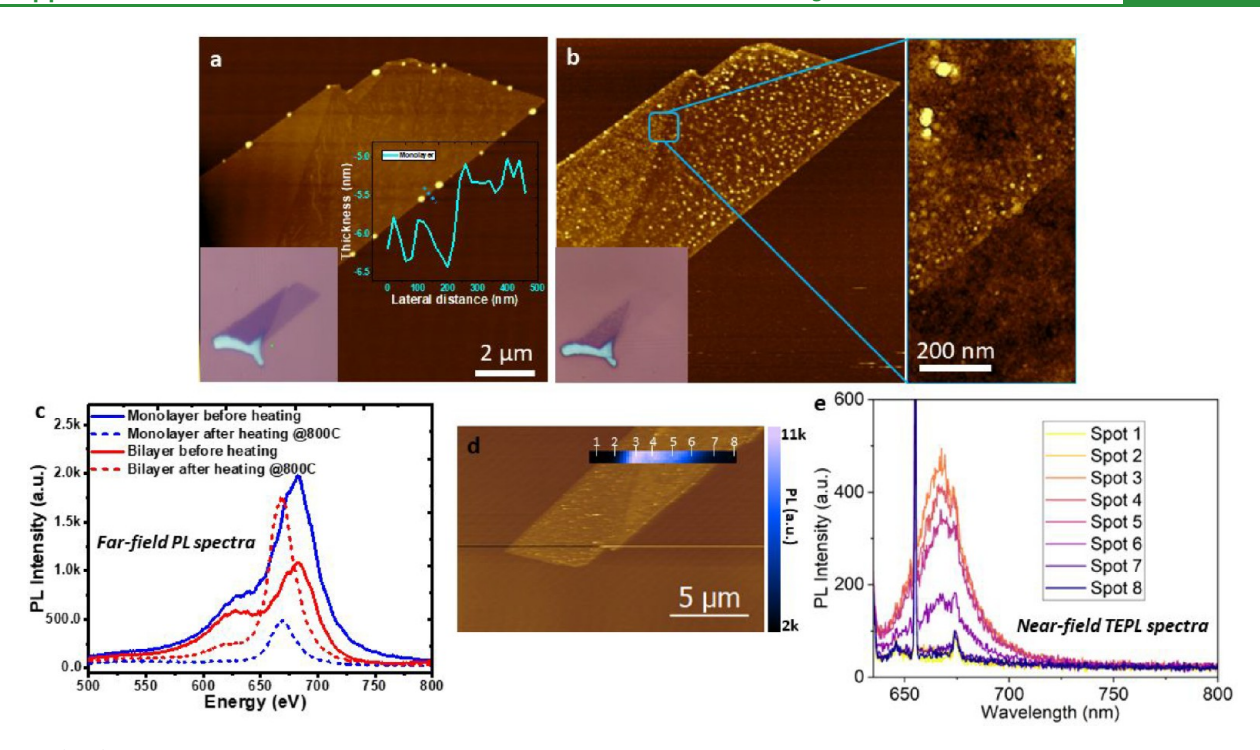


Figure 5. (a, b) AFM height images of the MoS₂ flake before and after the *ex situ* rapid thermal heating at a temperature of 800 °C for 45 s, respectively. Insets show the respective optical micrographs. The high-magnification AFM height image is also shown on the right side of (b), showing the morphology of both the monolayer (bottom section) as well as the bilayer (top section) after thermolysis. (c) Far-field PL spectra plotted for the *ex situ* thermolysis (pre- and post-heating at 800 °C for 45 s), where we can see the energy shift along with an increase in the emission intensity. (d) Near-field tip-enhanced PL spectroscopy carried out to measure emission characteristics of as-formed nanoparticles and a locally attached spatially resolved TEPL spectral map. (e) Point spectra from several points in the TEPL map from the high-intensity region in the center shown in (d).

the ${\rm MoS}_2$ nanoparticles is relatively uniform and varies on the order of 1%. Assuming there are no electromagnetic fields in the material, this would suggest that the contrast in the DPC image arises mainly due to small differences in crystallographic orientation. This could be consistent with our previous observations of variations of tilt in neighboring crystals of PtSe₂ formed by thermolysis. ²⁶

Nonequilibrium thermolysis leads to several phenomena including vacancy creation and migration (especially Svacancies), structural reconstruction, phase changes, and stoichiometric variations. Here, we used a confined configuration of 2D materials undergoing rapid thermolysis to more closely examine these phenomena that occur during nonequilibrium thermolysis. To create this configuration, we added a protective h-BN layer on top of the h-BN/MoS₂ configuration (shown thus far in Figures 1-3), thereby completely enclosing the MoS₂ flake (as shown in the atomic model in Figure 4a). The resulting encapsulated configuration is also shown in Figure S15 in the Supporting Information. Rapid heating was then performed to induce nonequilibrium thermolysis on this MoS₂ flake, which was encapsulated by a few-layer h-BN from both the top and bottom (h-BN/MoS₂/ h-BN), creating a closed "subpicoliter reactor" system. The dark-field STEM image in Figure 4b shows that the disintegrated MoS₂ contains both monolayer and few-layer regions (marked with two different colors). A magnified, highresolution HAADF-STEM image of the monolayer region (Figure 4c) reveals the formation of nanoparticles in pockets, similar to the nonconfined h-BN/MoS₂ configuration. The encapsulated system experiences additional pressure from the top and bottom few layers of h-BN, which affects the

thermolysis process. This increased pressure causes the temperature at which the nanoparticles form to increase (see Figures S16-S18). This is because the log of the diffusion coefficient decreases as a function of pressure proportional to the activation volume, 27,28 raising the temperature at which the transformation occurs. The closed "subpicoliter reactor" also helps maintain the stoichiometry of the formed nanoparticles, since they prevent chalcogen escape. Further, by increasing the duration of the peak thermolysis process time, we observe complete thermolysis in the encapsulated region, forming crystalline particles while simultaneously also observing that the adjacent unencapsulated monolayer becomes thicker and turns completely metallic due to chalcogen sublimation (see Figures S17c-e and S18). In contrast to the monolayer regions, we observed unique occurrences in the case of fewlayer regions (as shown in Figure 4d). A high-magnification HAADF-STEM image shows the formation of faceted trenches with mostly triangular or trapezoidal shapes (Figure S19). The preferentially oriented trench formation (see Figure 4d inset) under complete confinement suggests that line defects are likely contributing to the edge restructuring process. Previous studies have identified various types of edges in 2D TMDC layers after high-temperature treatment. Figure 4e shows the atomically resolved structural arrangement of bundled edges on one side of the trenches. The other sides of the trenches appear normal with no atomic accumulation. The unique edge restructuring observed in this study can be attributed to the confinement in the z-direction, which prevents atoms from migrating from one layer to another in a few-layer 2D system, leading to the formation of edge

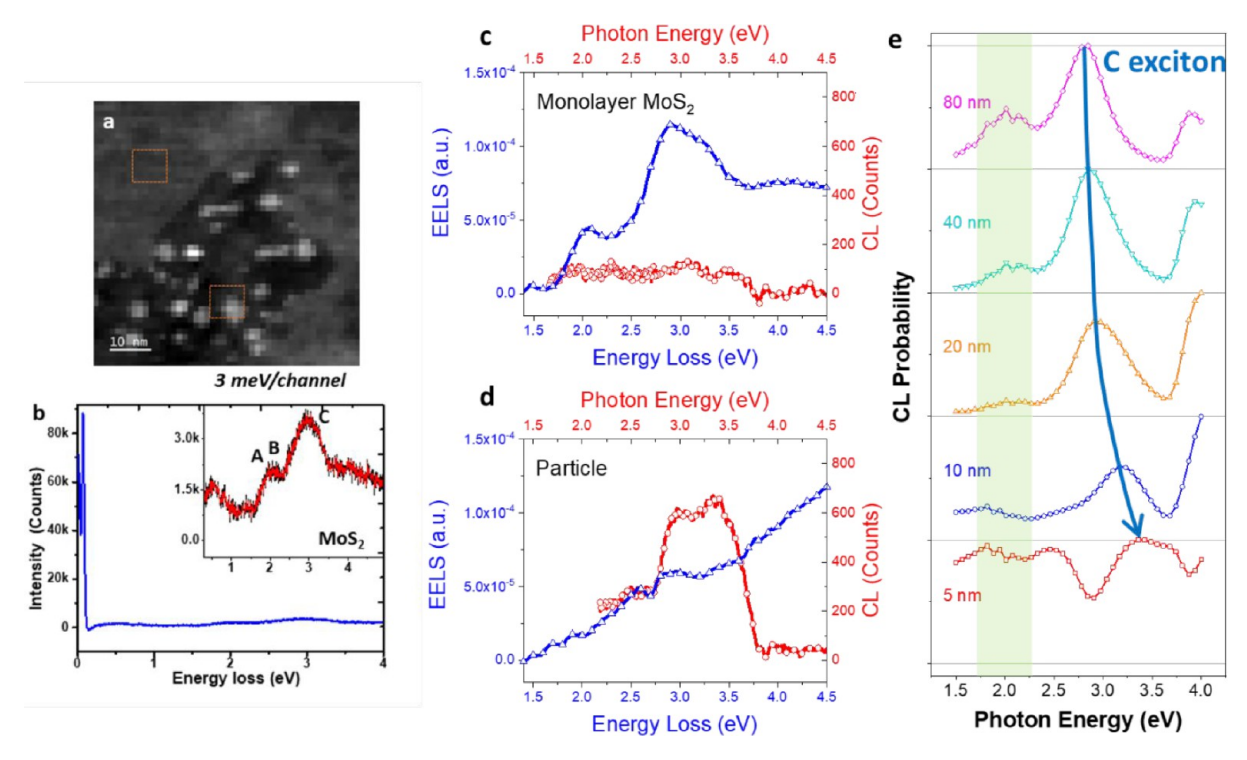


Figure 6. EELS and cathodoluminescence (CL) analysis of the MoS₂ nanoparticles performed before and after thermolysis (*in situ* heating). (a) HAADF-STEM image of as-heated MoS₂ and (b) corresponding EELS spectral response taken from the marked rectangular regions. The inset shows the magnified view of the valence-edge EELS spectra referring to A, B, and C excitons of the MoS₂ layer. (c) Spatially correlative EELS (blue, triangles) and CL (red, circles) spectra from the monolayer MoS₂ before rapid thermolysis. (d) Post-thermolysis of encapsulated monolayer MoS₂, with spatially correlative EELS (blue, triangles) and CL (red, circles) spectra for the as-formed MoS₂ particle region. (e) Theoretical prediction calculated using the boundary element method for a MoS₂ disk (1 nm in thickness) with a diameter of 80 nm (magenta, rhombuses), 40 nm (turquoise, downward triangles), 20 nm (orange, upward triangles), 10 nm (blue, circles), and 5 nm (red, squares) supported by a h-BN substrate (1 nm in thickness).

bundling. This unique phenomenon merits further detailed investigation but is beyond the scope of this manuscript.

To further evaluate the shape stability of the disintegrated particles, we used density functional theory (DFT, nudged elastic band method) to analyze the different shapes obtained. We found that the nonconfined configuration tended to form circular or hexagonal shapes, while the confined and encapsulated configurations resulted in slower, stoichiometric transformation and the formation of thermodynamically stable, triangular shapes in the case of 3-fold symmetric MoS₂. Considering the nanoparticle formation process, there are two main driving forces for nanoparticle shape evolution: (1) diffusion of atoms at the particle surface/edge and (2) solidstate reaction of TMDC decomposition at the surface/edge. Under diffusion-limited kinetics, the nanoparticle shape will be determined by the diffusion coefficient anisotropy, whereas under reaction-rate-limited kinetics, the nanoparticle shape will be determined by the anisotropy of the TMDC's decomposition reaction. Figure 4f shows the simulated diffusion coefficient anisotropy for a number of edge geometries. The results are consistent with diffusion-limited kinetics in the confined geometry. On the other hand, nanoparticles formed in the nonconfined geometry exhibit very little anisotropy. We can rationalize this by considering the effect of h-BN encapsulation as an effective pressure increase, which decreases the diffusion coefficient and results in diffusion-limited shape evolution. If diffusion is relatively fast compared to evaporation, the shape will be closer to the thermodynamic equilibrium shape (a triangle due to the 3-fold symmetry of MoS_2). If not, the shape will be closer to the kinetic shape (more round or dendritic). Fast diffusion along the edge is possible at high temperatures (with an energy barrier of 0.8 eV), leading to shape changes that are closer to the thermodynamic equilibrium shape (Figure 4f). Intermediate energy states for sulfur diffusion at the MoS_2 edge are shown in Figures S20 and S21.

Investigating the optical characteristics of the nanoparticles produced in our study was challenging by using the in situ MEMS grid. The freestanding SiN_x membrane has overlapping background emission spectra (likely from defects and its nonstoichiometry), and in addition, its nonreflective surfaces do not allow for a sufficient signal to be distinguished between the emitting nanoparticles and the background when using micro-PL spectroscopy. The near-field spectral luminescence measurement was also unsuccessful due to the freestanding SiN_x membrane interaction with the gold-coated near-field tip. We optimized the thermolysis process using an ex situ approach to address this issue and develop a more scalable method for producing nanoparticles (see Materials and Methods for more details). The ex situ approach, which involves rapid thermal annealing (RTA), produced identical quantum particles and allowed for their characterization using both far-field and near-field micro-PL spectroscopy. Figure 5a,b shows AFM height images of a MoS₂ monolayer (includes partly bilayer as well) before and after being heated at 800 °C for 45 s (inside a customized furnace-based RTA system), showing the topography before and after ex situ thermolysis. A noticeable structural evolution is visible throughout the MoS₂

flake upon comparison of the two images. Finding the optimal conditions for producing nanoparticles is challenging, as the formation of defect-mediated intact nanoparticles requires a narrow window, with either too many defects leading to particle destruction or slow evaporation leading to the formation of metal nanoclusters. Structural transformation is more pronounced at the monolayer edge and monolayerbilayer interface due to the higher reactivity of these sites as predicted by theoretical energy calculations. 31-34 Additionally, the bright dots in the AFM image are Mo clusters rather than MoS₂ nanoparticles in some parts of the flake due to the complete loss of sulfur atoms during the longer heating process. We adopted a slightly longer (45 s) heating time to ensure complete transformation (see Table S1 and Figure S22 for complete optimization results). A complete transformation occurs in the monolayer case, while a few layers undergo thermolysis with the remaining underlying layer and nanoparticle formation under the same temperature and conditions.

The blue shift in the PL spectra of the monolayer and bilayer cases, shown in Figure 5c, suggests the formation of defectmediated nanoparticle emission, consistent with previously reported quantum dots³⁵ while in contrast with the emitters based on 2D materials.^{6,36} However, many areas of the flake show near-zero PL emission, particularly in areas that have undergone overheating (Figure S22). A deconvoluted plot of the monolayer before heating (solid blue spectrum in Figure 5c) is shown in Figure S23. To study the localized emission properties of the nanoparticles, we used near-field tipenhanced photoluminescence spectroscopy (TEPL). This technique provides high resolution, in terms of spatial variations and localized emission features from the active material region. Figure 5d shows the overlapped spatially mapped TEPL signal of the transformed regions after ex situ thermolysis with the AFM topography image. A comparison of the TEPL spectral response from a few spots in the center of the flake (Figure 5e) shows no significant peak shift in relation to the far-field PL (Figure 5c). A quenched PL signal is observed toward the flake edges, suggesting the formation of thicker, multilayer particles that appear bright in AFM topography images. More transformation (conversion into metallic Mo particles) occurred at the edges compared to the center positions under the optimized ex situ RTA processing. However, further studies and optimization may be necessary to fine-tune the controlled nanoparticle formation and simultaneously avoid the formation of bulk metal particles (see Figure S24 for MoSe₂).

To understand the defect-mediated emission of MoS₂ after thermolysis, we probe the excitation of valence electrons using electron energy loss spectroscopy (EELS) in a state-of-the-art probe-corrected STEM with a highly coherent and monochromatic electron source. The electron energy losses associated with A, B, and C excitons of MoS2 are identified in both the confined nanoparticle and the film after the thermolysis, in reference to the simultaneously measured h-BN polariton peak position (Figure 6a,b and Figure S25). Although the post-thermolysis intensity is attenuated (prethermolysis intensity is not shown here), the EELS result suggests a similar light extinction property before and after the thermolysis. The extinction of nanoparticles is known as a combined effect of energy absorption and scattering,³⁷ which is sensitive to the particle's geometry and dielectric environment at the single-particle level. 22 Therefore, we adopt a multimodal approach to measure the electron-beam-excited scattering, i.e.,

cathodoluminescence (CL) that is spatially correlated with EELS in a TEM with a custom-built optical spectroscopy system.³⁸ For the monolayer MoS₂ encapsulated by h-BN before and after the thermolysis, we confirm that the EELS peaks of A, B, and C excitons (blue solid curves, Figure 6 c,d) still exist but are attenuated. Concurrently, the CL indicates a strong encapsulation-induced bulk excitonic emission (red solid curves, Figure 6d), while direct band edge emission is not present (Figure S26a). Enhanced C exciton emission that is higher in energy concurrent with a lack of primary A or B exciton emission implies that the highly confined, high-energy excitons resonating within the particles have insufficient time or phonon interactions to relax into a lower energy state, causing them to emit at this higher energy state. This agrees with our theoretical prediction using the boundary element method (Figure S27) that shows the quenched A and B excitons (green shadowed spectral range in Figure 6e) as well as the blue-shifted C exciton (blue arrow in Figure 6e) in CL emission from a MoS₂ disk supported by h-BN.³⁹ Similar emission characteristics are seen in the film region of Figure 6a (Figure S26), suggesting that such a region may mainly consist of nanoparticles with a background intact layer of MoS₂ resulting from incomplete thermolysis.

CONCLUSIONS

In conclusion, we have demonstrated sub-10 nm uniform particle formation via thermolysis of a single-crystalline monolayer and few-layer TMDC flakes with h-BN supported as well as in an encapsulated van der Waals heterostructure. The h-BN supported TMDC monolayer undergoes a uniform NP formation having an average diameter of ~5 nm, while with the few-layer case, it is closer to ~10 nm. The encapsulation is observed to suppress thermolysis temperature requirements and leads to the formation of highly crystalline and stoichiometric nanoparticles. The formed nanoparticles exhibit electronic signatures different from those of bulk 2D TMDCs, though no distinct signatures of quantum confinement were observed in either photoluminescence or cathodoluminescence spectroscopy. In summary, our work opens a new route to producing crystalline 0D and 1D nanostructures from 2D van der Waals layers and allows the study of phase transformation and diffusion phenomena in solid-state systems in highly confined and extreme environments.

■ MATERIALS AND METHODS

Materials Synthesis. A mechanical exfoliation technique is used to make the monolayer as well as the few-layered TMDCs (MoS₂, MoSe₂, WS₂, WSe₂) and few-layered h-BN. After confirmation of the thin exfoliated layers using an optical microscope, the mixture was then transferred to the target MEMS heating chip. The site-specific targeted transfer was achieved by the PDMS-based dry transfer technique.²³ All of the transfer was precisely done to make sure the TMDC layers face freestanding regions to achieve atomic-resolution STEM microscopy. Once a TMDC or h-BN layer was transferred to the MEMS chip over the located freestanding SiN_x membrane area, it was then annealed in forming gas up to 300 °C for 12–15 h to reduce the PDMS contaminants which were left over during the dry transfer technique. Successively the next TMDC or h-BN layer was transferred further to synthesize the confined configuration like h-BN/MoS₂/h-RN

Material Processing. As-received, prefabricated heating chips (MEMS-based) were taken to the focus ion beam (FIB) chamber to fabricate holes in the TEM transmitting area. Very precise and site-

specific submicron holes were made into SiNx membranes using the Xe-plasma-based FIB technique (TESCAN S8000X focused ion beam/scanning electron microscope). FIB drilling used 5 pA current at 10 kV accelerating voltage to substantially reduce the redeposition process as well as reduction of ion beam induced damage. The in situ thermolysis process was achieved using a prefabricated MEMS heating chip loaded into an in situ vacuum heating TEM holder (Hummingbird Scientific LLC, USA). The rate of heating was ultrafast, and the target temperature was achieved in a few seconds at the rate of 100 °C/s; similarly, the cooling rate was achieved as well. Ex situ thermolysis was performed in a custom-made rapid thermal annealing system. The single-zone quartz-tube-based heating furnace (ThermoFisher Scientific, Lindberg Mini) was converted into a rapid thermal system. A target temperature (processing of the 2D layer) was first maintained for a few minutes in a continuous Ar-flowing quartz tube (before the quartz tube was evacuated and flushed with Ar gas multiple times using a rotary pump). A quartz rod with an attached sample holder was used to insert and withdraw quickly in and out of the hot zone (where the target temperature was maintained) within a frame of seconds. Several cycles of processing were done to reach the as-optimized target temperature and thermolysis time to achieve quantum particle formation (see detailed parameters in Table S1). Each optimization process needed several steps including exfoliation of fresh TMDC layers, dry transfer to SiO₂/Si substrate, forming gas based annealing treatment, AFM and optical microscopy characterization before and after thermolysis, and micro-PL/Raman spectroscopic analysis.

Material Characterization. An in situ TEM vacuum heating holder from Hummingbird Scientific LLC was used to perform all the in situ thermolysis processes and analyses. Transmission electron microscopy (TEM) and scanning transmission electron microscopy (STEM) techniques were used to do all the in situ thermolysis processing. A JEOL JEM 200 microscope with 200 kV accelerating voltage was utilized for all the TEM/STEM and 4D-STEM analyses. For 4D-STEM, data were collected using STEMx (Gatan) with a Gatan OneView camera (4k × 4k) using drift correction once every row. A 10 μ m condenser aperture was used for 4D-STEM experiments to limit overlap between diffraction disks. 4D-STEM DPC mapping was performed by measuring beam displacement using the center-of-mass method. The Gatan Microscopy Suite (GMS v3) was used to analyze the strain. To avoid any beam damage and irradiation effect, we kept changing the image acquisition positions as much as possible for every scan. Probe-corrected STEM (JEOL NEO ARM 200) was used to acquire atomic-resolved dark- and bright-field STEM images. EDS mapping was done with a NEO-ARM 200 instrument containing a high-speed dual detector which facilitated fast acquisition with high gain, helpful for beam-sensitive material analysis. Further, valence band-edge EELS analysis was done using a NION Ultra-STEM 100 system having a monochromatic electron source with an inverted e-gun configuration used to resolve the A, B, and C excitons. The band-edge EELS spectra were referenced with respect to h-BN phonon lines. EELS was measured at an 80 keV accelerating voltage and 0.75 pm probe size which attained a 35 meV zero loss feature. Cathodoluminescence (CL) along with EELS spectra were recorded using an environmental TEM equipped with a monochromated Schottky field-emission gun (FEG) at 80 kV accelerating voltage and ~1 nm probe size, which obtained an energy spread of 80 meV. The spatially correlative measurement of EELS and CL was achieved using a custom-built optical spectroscopy system that inserted a parabolic mirror into the narrow gap between the sample holder and the lower polepiece of the objective lens.

Image segmentation and nanoparticle measurement were performed using a series of filters and morphological operations were performed using the Scikit-image Python library. 40 HAADF-STEM images were initially processed using a Gaussian filter, followed by morphological reconstruction using dilation and erosion. This produced a nearly binary version of the STEM image, which could be finally segmented using an Otsu threshold. A connected component algorithm was used to link individually segmented pixels in particles, which could then be measured and analyzed.

Theoretical Modeling. Here, we utilized the climbing image nudged elastic band method⁴¹ to calculate the energy barrier for S-vacancy diffusion. The system was modeled by a ribbon with a S-vacancy located at the edge (see the Figure S20 for the full structure). We performed DFT calculations using VASP software $^{42-44}$ with a 400 eV energy cutoff, the PBE functional and D3 method for vdW correction, $^{45-47}$ and $3\times3\times1$ k-point grid. The initial state, final state, and other states in between are shown in Figure 4f. We saw two saddle points and a local minimum (intermediate state) between these two saddle points. Taking this intermediate state as the final structure, we again performed NEB calculations with 10 additional states between the initial state and the intermediate state. The energy profile of this reaction pathway showed a saddle point with a reaction barrier of 0.8 eV exactly at the middle, as shown in Figure S21.

ASSOCIATED CONTENT

Supporting Information

The Supporting Information is available free of charge at https://pubs.acs.org/doi/10.1021/acsami.3c13471.

Information on *in situ* and *ex situ* processing techniques, details of MEMS heating TEM chip, optical microscopic images of the fabrication of encapsulated configuration, TEM and STEM images before and after *in situ* heating of the h-BN/MoS₂ and h-BN/MoS₂/h-BN configurations, edge reconstructions by atomically resolved HAADF-STEM images, nanoscale EDS mapping, DFT calculations for the edge vacancies and formation energies, near-field TEPL spectra for MoSe₂, and cathodoluminescence measurements and their fitting/analysis (PDF)

AUTHOR INFORMATION

Corresponding Authors

Eric A. Stach — Materials Science and Engineering, University of Pennsylvania, Philadelphia, Pennsylvania 19104, United States; orcid.org/0000-0002-3366-2153; Email: stach@seas.upenn.edu

Deep Jariwala — Electrical and Systems Engineering, University of Pennsylvania, Philadelphia, Pennsylvania 19104, United States; orcid.org/0000-0002-3570-8768; Email: dmj@seas.upenn.edu

Authors

Pawan Kumar — Electrical and Systems Engineering and Materials Science and Engineering, University of Pennsylvania, Philadelphia, Pennsylvania 19104, United States; Inter-university Microelectronics Center (IMEC), Leuven 3001, Belgium; ⊚ orcid.org/0000-0002-5764-2915

Jiazheng Chen — Electrical and Systems Engineering, University of Pennsylvania, Philadelphia, Pennsylvania 19104, United States

Andrew C. Meng — Materials Science and Engineering, University of Pennsylvania, Philadelphia, Pennsylvania 19104, United States; Department of Physics and Astronomy, University of Missouri, Columbia, Missouri 65211, United States; © orcid.org/0000-0002-3060-8928

Wei-Chang D. Yang — National Institute of Standards and Technology, Gaithersburg, Maryland 20899, United States; orcid.org/0000-0002-7481-7916

Surendra B. Anantharaman — Electrical and Systems Engineering, University of Pennsylvania, Philadelphia, Pennsylvania 19104, United States; Low-dimensional Semiconductors Lab, Metallurgical and Materials

- Engineering, Indian Institute of Technology-Madras, Chennai, Tamilnadu 600036, India
- James P. Horwath Materials Science and Engineering, University of Pennsylvania, Philadelphia, Pennsylvania 19104, United States; Argonne National Laboratory, Lemont, Illinois 60439, United States; orcid.org/0000-0002-7333-3768
- Juan C. Idrobo Center for Nanophase Materials Sciences, Oak Ridge National Laboratory, Oak Ridge, Tennessee 37830, United States; Materials Science & Engineering, University of Washington, Seattle, Washington 98195, United States; Occid.org/0000-0001-7483-9034
- Himani Mishra Department of Mechanical Engineering and Texas Materials Institute, University of Texas, Austin, Texas 78712, United States
- Yuanyue Liu Department of Mechanical Engineering and Texas Materials Institute, University of Texas, Austin, Texas 78712, United States
- Albert V. Davydov National Institute of Standards and Technology, Gaithersburg, Maryland 20899, United States

Complete contact information is available at: https://pubs.acs.org/10.1021/acsami.3c13471

Notes

The authors declare no competing financial interest.

■ ACKNOWLEDGMENTS

D.J., E.A.S., and P. K. acknowledge primary support from the National Science Foundation (DMR-1905853) and support from University of Pennsylvania Materials Research Science and Engineering Center (MRSEC) (DMR-1720530) in addition to usage of MRSEC-supported facilities. The sample fabrication, assembly, and characterization were carried out at the Singh Center for Nanotechnology at the University of Pennsylvania, which is supported by the National Science Foundation (NSF) National Nanotechnology Coordinated Infrastructure Program grant NNCI-1542153. D.J. also acknowledges partial support for this work by the Air Force Office of Scientific Research (AFOSR) FA2386-20-1-4074. Y. L. acknowledges the support by Welch Foundation (Grant No. F-1959-20180324). Certain equipment, instruments, software, or materials, commercial or noncommercial, are identified in this paper in order to specify the experimental procedure adequately. Such identification is not intended to imply recommendation or endorsement of any product or service by NIST, nor is it intended to imply that the materials or equipment identified are necessarily the best available for the purpose. A portion of the STEM research was conducted as part of a user project at the Center for Nanophase Materials Sciences (CNMS), which is a US Department of Energy, Office of Science User Facility at Oak Ridge National Laboratory (ORNL).

REFERENCES

- (1) Fu, J.-H.; Min, J.; Chang, C.-K.; Tseng, C.-C.; Wang, Q.; Sugisaki, H.; Li, C.; Chang, Y.-M.; Alnami, I.; Syong, W.-R.; Lin, C.; Fang, F.; Zhao, L.; Lo, T.-H.; Lai, C.-S.; Chiu, W.-S.; Jian, Z.-S.; Chang, W.-H.; Lu, Y.-J.; Shih, K.; Li, L.-J.; Wan, Y.; Shi, Y.; Tung, V. Oriented Lateral Growth of Two-dimensional Materials on c-plane Sapphire. *Nat. Nanotechnol.* **2023**, *18*, 1289.
- (2) Stanford, M. G.; Rack, P. D.; Jariwala, D. Emerging Nanofabrication and Quantum Confinement Techniques for 2D

- materials Beyond Graphene. npj 2D Materials and Applications 2018, 2 (1), 20.
- (3) Peyskens, F.; Chakraborty, C.; Muneeb, M.; Van Thourhout, D.; Englund, D. Integration of Single Photon Emitters in 2D Layered Materials with a Silicon Nitride Photonic Chip. *Nat. Commun.* **2019**, *10* (1), 4435.
- (4) Li, Z.; Wang, T.; Miao, S.; Lian, Z.; Shi, S.-F. Fine Structures of Valley-polarized Excitonic States in Monolayer Transitional Metal Dichalcogenides. *Nanophotonics* **2020**, *9* (7), 1811–1829.
- (5) Xu, D. D.; Vong, A. F.; Lebedev, D.; Ananth, R.; Wong, A. M.; Brown, P. T.; Hersam, M. C.; Mirkin, C. A.; Weiss, E. A. Conversion of Classical Light Emission from a Nanoparticle-Strained WSe2Monolayer into Quantum Light Emission via Electron Beam Irradiation. *Adv. Mater.* 2023, 35 (5), No. 2208066.
- (6) Kim, G.; Kim, H. M.; Kumar, P.; Rahaman, M.; Stevens, C. E.; Jeon, J.; Jo, K.; Kim, K.-H.; Trainor, N.; Zhu, H.; Sohn, B.-H.; Stach, E. A.; Hendrickson, J. R.; Glavin, N. R.; Suh, J.; Redwing, J. M.; Jariwala, D. High-Density, Localized Quantum Emitters in Strained 2D Semiconductors. ACS Nano 2022, 16 (6), 9651–9659.
- (7) Ozdemir, N. K.; Cline, J. P.; Kiely, C. J.; McIntosh, S.; Snyder, M. A. Scalable Biomineralization of CdS Quantum Dots by Immobilized Cystathionine γ -Lyase. ACS Sustainable Chem. Eng. **2020**, 8 (40), 15189–15198.
- (8) Shen, J.; He, Y.; Wu, J.; Gao, C.; Keyshar, K.; Zhang, X.; Yang, Y.; Ye, M.; Vajtai, R.; Lou, J.; Ajayan, P. M. Liquid Phase Exfoliation of Two-Dimensional Materials by Directly Probing and Matching Surface Tension Components. *Nano Lett.* **2015**, *15* (8), 5449–5454.
- (9) Brent, J. R.; Savjani, N.; O'Brien, P. Synthetic Approaches to Two-dimensional Transition Metal Dichalcogenide Nanosheets. *Prog. Mater. Sci.* **2017**, *89*, 411–478.
- (10) Duan, Z.; Chen, T.; Shi, J.; Li, J.; Song, K.; Zhang, C.; Ding, S.; Li, B.; Wang, G.; Hu, S.; He, X.; He, C.; Xu, H.; Liu, X.; Jin, C.; Zhong, J.; Hao, G. Space-confined and Substrate-directed Synthesis of Transition-metal Dichalcogenide Nanostructures with Tunable Dimensionality. *Science Bulletin* **2020**, *65* (12), 1013–1021.
- (11) Huang, P.-Y.; Qin, J.-K.; Zhu, C.-Y.; Zhen, L.; Xu, C.-Y. 2D–1D Mixed-dimensional Heterostructures: Progress, Device Applications and Perspectives. *J. Phys.: Condens. Matter* **2021**, 33 (49), 493001.
- (12) Liao, L.; Lin, Y.-C.; Bao, M.; Cheng, R.; Bai, J.; Liu, Y.; Qu, Y.; Wang, K. L.; Huang, Y.; Duan, X. High-speed Graphene Transistors with a Self-aligned Nanowire Gate. *Nature* **2010**, *467* (7313), 305–308.
- (13) Wang, R.; Wang, T.; Hong, T.; Xu, Y.-Q. Probing Photoresponse of Aligned Single-walled Carbon Nanotube Doped Ultrathin MoS2. *Nanotechnology* **2018**, 29 (34), 345205.
- (14) Chen, X.; Jiang, B.; Wang, D.; Li, G.; Wang, H.; Wang, H.; Wang, F.; Wang, P.; Liao, L.; Wei, Z. Gate-tunable the Interface Properties of GaAs—WSe2 (1D—2D) vdWs Heterojunction for Highresponsivity, Self-powered Photodetector. *Appl. Phys. Lett.* **2021**, *118* (4), 041102.
- (15) Sang, X.; Li, X.; Puretzky, A. A.; Geohegan, D. B.; Xiao, K.; Unocic, R. R. Atomic Insight into Thermolysis-Driven Growth of 2D MoS2. Adv. Funct. Mater. 2019, 29 (52), No. 1902149.
- (16) Fei, L.; Lei, S.; Zhang, W.-B.; Lu, W.; Lin, Z.; Lam, C. H.; Chai, Y.; Wang, Y. Direct TEM Observations of Growth Mechanisms of Two-dimensional MoS2 Flakes. *Nat. Commun.* **2016**, *7* (1), 12206.
- (17) Kumar, P.; Horwath, J. P.; Foucher, A. C.; Price, C. C.; Acero, N.; Shenoy, V. B.; Stach, E. A.; Jariwala, D. Direct Visualization of Out-of-equilibrium Structural Transformations in Atomically Thin Chalcogenides. *npj* 2D Materials and Applications 2020, 4 (1), 16.
- (18) Hages, C. J.; Levcenco, S.; Miskin, C. K.; Alsmeier, J. H.; Abou-Ras, D.; Wilks, R. G.; Bär, M.; Unold, T.; Agrawal, R. Improved Performance of Ge-alloyed CZTGeSSe Thin-film Solar Cells through Control of Elemental Losses. *Progress in Photovoltaics: Research and Applications* 2015, 23 (3), 376–384.
- (19) Yang, W.-C.; Miskin, C. K.; Carter, N. J.; Agrawal, R.; Stach, E. A. Compositional Inhomogeneity of Multinary Semiconductor

- Nanoparticles: A Case Study of Cu2ZnSnS4. Chem. Mater. 2014, 26 (24), 6955-6962.
- (20) Hages, C. J.; Koeper, M. J.; Miskin, C. K.; Brew, K. W.; Agrawal, R. Controlled Grain Growth for High Performance Nanoparticle-Based Kesterite Solar Cells. *Chem. Mater.* **2016**, 28 (21), 7703–7714.
- (21) Rosenberger, M. R.; Chuang, H.-J.; McCreary, K. M.; Hanbicki, A. T.; Sivaram, S. V.; Jonker, B. T. Nano-"Squeegee" for the Creation of Clean 2D Material Interfaces. ACS Appl. Mater. Interfaces 2018, 10 (12), 10379–10387.
- (22) Chen, S.; Son, J.; Huang, S.; Watanabe, K.; Taniguchi, T.; Bashir, R.; van der Zande, A. M.; King, W. P. Tip-Based Cleaning and Smoothing Improves Performance in Monolayer MoS2 Devices. *ACS Omega* **2021**, *6* (5), 4013–4021.
- (23) Garcia, A.; Raya, A. M.; Mariscal, M. M.; Esparza, R.; Herrera, M.; Molina, S. I.; Scavello, G.; Galindo, P. L.; Jose-Yacaman, M.; Ponce, A. Analysis of Electron Beam Damage of Exfoliated MoS2 Sheets and Quantitative HAADF-STEM Imaging. *Ultramicroscopy* **2014**, *146*, 33–38.
- (24) Ophus, C. Four-Dimensional Scanning Transmission Electron Microscopy (4D-STEM): From Scanning Nanodiffraction to Ptychography and Beyond. *Microscopy and Microanalysis* **2019**, 25 (3), 563–582.
- (25) Hachtel, J. A.; Idrobo, J. C.; Chi, M. Sub-Ångstrom Electric Field Measurements on a Universal Detector in a Scanning Transmission Electron Microscope. *Advanced Structural and Chemical Imaging* **2018**, *4* (1), 10.
- (26) Kumar, P.; Meng, A. C.; Jo, K.; Stach, E. A.; Jariwala, D. Interfacial Reaction and Diffusion at the One-Dimensional Interface of Two-Dimensional PtSe2. *Nano Lett.* **2022**, *22* (12), 4733–4740.
- (27) W. Balluffi, R.; M. Allen, S.; Craig Carter, W. The Diffusion Equation. In *Kinetics of Materials*; Wiley: 2005; pp 77–97.
- (28) Shewmon, P. G. Diffusion in Solids; McGraw-Hill: 1963; Solid-State Electronics, Vol. 7.
- (29) Hu, G.; Fung, V.; Sang, X.; Unocic, R. R.; Ganesh, P. Predicting Synthesizable Multi-functional Edge Reconstructions in Two-dimensional Transition Metal Dichalcogenides. *npj Computational Materials* **2020**, *6* (1), 44.
- (30) Sang, X.; Li, X.; Zhao, W.; Dong, J.; Rouleau, C. M.; Geohegan, D. B.; Ding, F.; Xiao, K.; Unocic, R. R. In Situ Edge Engineering in Two-dimensional Transition Metal Dichalcogenides. *Nat. Commun.* **2018**, 9 (1), 2051.
- (31) Hao, Y.; Xu, L.-C.; Pu, J.; Wang, L.; Huang, L.-F. Stable Zigzag Edges of Transition-metal Dichalcogenides with High Catalytic Activity for Oxygen Reduction. *Electrochim. Acta* **2020**, 338, No. 135865.
- (32) Jaramillo, T. F.; Jørgensen, K. P.; Bonde, J.; Nielsen, J. H.; Horch, S.; Chorkendorff, I. Identification of Active Edge Sites for Electrochemical H2 Evolution from MoS2 Nanocatalysts. *Science* **2007**, 317 (5834), 100–102.
- (33) Zhang, F.; Lu, Z.; Choi, Y.; Liu, H.; Zheng, H.; Xie, L.; Park, K.; Jiao, L.; Tao, C. Atomically Resolved Observation of Continuous Interfaces between an As-Grown MoS2Monolayer and a WS2/MoS2 Heterobilayer on SiO2. ACS Applied Nano Materials 2018, 1 (5), 2041–2048.
- (34) Longo, R. C.; Addou, R.; Kc, S.; Noh, J.-Y.; Smyth, C. M.; Barrera, D.; Zhang, C.; Hsu, J. W. P.; Wallace, R. M.; Cho, K. Intrinsic Air Stability Mechanisms of Two-dimensional Transition Metal Dichalcogenide Surfaces: Basal versus Edge Oxidation. 2D Materials 2017, 4 (2), No. 025050.
- (35) Golovynskyi, S.; Bosi, M.; Seravalli, L.; Li, B. MoS2 Two-dimensional Quantum Dots with Weak Lateral Quantum Confinement: Intense Exciton and Trion Photoluminescence. *Surfaces and Interfaces* **2021**, 23, No. 100909.
- (36) Chakraborty, C.; Vamivakas, N.; Englund, D. Advances in Quantum Light Emission from 2D materials. *Nanophotonics* **2019**, 8 (11), 2017–2032.
- (37) Losquin, A.; Zagonel, L. F.; Myroshnychenko, V.; Rodríguez-González, B.; Tencé, M.; Scarabelli, L.; Förstner, J.; Liz-Marzán, L.

- M.; García de Abajo, F. J.; Stéphan, O.; Kociak, M. Unveiling Nanometer Scale Extinction and Scattering Phenomena through Combined Electron Energy Loss Spectroscopy and Cathodoluminescence Measurements. *Nano Lett.* **2015**, *15* (2), 1229–1237.
- (38) Yoon, Y.; Yang, W.-C. D.; Ha, D.; Haney, P. M.; Hirsch, D.; Yoon, H. P.; Sharma, R.; Zhitenev, N. B. Unveiling Defect-Mediated Charge-Carrier Recombination at the Nanometer Scale in Polycrystalline Solar Cells. ACS Appl. Mater. Interfaces 2019, 11 (50), 47037–47046.
- (39) Waxenegger, J.; Trügler, A.; Hohenester, U. Plasmonics Simulations with the MNPBEM Toolbox: Consideration of Substrates and Layer Structures. *Comput. Phys. Commun.* **2015**, *193*, 138–150.
- (40) van der Walt, S.; Schonberger, J. L.; Nunez-Iglesias, J.; Boulogne, F.; Warner, J. D.; Yager, N.; Gouillart, E.; Yu, T. Scikitimage: Image Processing in Python. *PeerJ.* **2014**, *2*, No. e453.
- (41) Henkelman, G.; Uberuaga, B. P.; Jónsson, H. A Climbing Image Nudged Elastic Band Method for Finding Saddle Points and Minimum Energy Paths. J. Chem. Phys. 2000, 113 (22), 9901–9904.
- (42) Kresse, G.; Hafner, J. Ab Initio Molecular Dynamics for Liquid Metals. *Phys. Rev. B* **1993**, *47* (1), 558–561.
- (43) Kresse, G.; Furthmüller, J. Efficiency of Ab-initio Total Energy Calculations for Metals and Semiconductors using a Plane-wave Basis Set. *Comput. Mater. Sci.* **1996**, *6* (1), 15–50.
- (44) Kresse, G.; Furthmüller, J. Efficient Iterative Schemes for Ab Initio Total-energy Calculations using a Plane-wave Basis Set. *Phys. Rev. B* **1996**, *54* (16), 11169–11186.
- (45) Grimme, S.; Ehrlich, S.; Goerigk, L. Effect of the Damping Function in Dispersion Corrected Density Functional Theory. *J. Comput. Chem.* **2011**, 32 (7), 1456–1465.
- (46) Grimme, S.; Antony, J.; Ehrlich, S.; Krieg, H. A Consistent and Accurate Ab Initio Parametrization of Density Functional Dispersion Correction (DFT-D) for the 94 Elements H-Pu. *J. Chem. Phys.* **2010**, 132 (15), 154104.
- (47) Kresse, G.; Joubert, D. From Ultrasoft Pseudopotentials to the Projector Augmented-wave Method. *Phys. Rev. B* **1999**, *59* (3), 1758–1775.